



# Effect of multiple parameters on the supersonic gas-jet target characteristics for laser wakefield acceleration

Qiu-Shi Liu<sup>1</sup> · Ming-Jiang Ma<sup>1</sup> · Bao-Zhen Zhao<sup>1</sup> · Xiao-Hua Zhang<sup>1</sup> · Chong Lv<sup>1</sup> · Xiang-Hao Meng<sup>1</sup> · Ji Zhang<sup>1</sup> · Xiao-Na Ban<sup>1</sup> · Zhao Wang<sup>1</sup> · Xiao-Feng Xi<sup>1</sup> · Bao-Xian Tian<sup>1</sup> · Chuang-Ye He<sup>1</sup> · Bing Guo<sup>1</sup>

Received: 30 March 2021 / Revised: 7 May 2021 / Accepted: 26 May 2021 / Published online: 19 July 2021

© China Science Publishing & Media Ltd. (Science Press), Shanghai Institute of Applied Physics, the Chinese Academy of Sciences, Chinese Nuclear Society 2021

**Abstract** The supersonic gas-jet target is an important experimental target for laser wakefield acceleration (LWFA), which has great potential for driving novel radiation sources such as betatron radiation and Compton scattering gamma rays. According to different electron acceleration requirements, it is necessary to provide specific supersonic gas jets with different density profiles to generate electron beams with high quality and high repetition rates. In this study, the interference images and density profiles of different gas-jet targets were obtained through a modified Nomarski interference diagnosis system. The relationships between the gas density and back pressure, nozzle structure, and other key parameters were studied. Targets with different characteristics are conducive to meeting the various requirements of LWFA.

**Keywords** Supersonic gas-jet target · Laser wakefield acceleration · Electron acceleration · Optical interference diagnosis

---

This work was supported by the Programs for the National Natural Science Foundation of China (Nos. 11975316, 11775312, 12005305 and 61905287) and the Continue Basic Scientific Research Project (Nos. WDJC-2019-02 and BJ20002501).

---

Qiu-Shi Liu  
liuqishi@ciae.ac.cn

✉ Bao-Zhen Zhao  
zhaobaozhen@ciae.ac.cn

✉ Bing Guo  
guobing@ciae.ac.cn

<sup>1</sup> Department of Nuclear Physics, China Institute of Atomic Energy, Beijing 102413, China

## 1 Introduction

With the development of chirped-pulse amplification (CPA) [1], the peak intensity of ultrashort pulse lasers has reached more than  $10^{18}$  W/cm<sup>2</sup>, which significantly promotes the research of novel particle accelerators driven by ultrashort and ultraintense lasers. The laser wakefield can provide a high acceleration gradient above 100 GV/m and produce high-quality GeV electron beams [2–4]. To date, the highest energy of electron beams accelerated by petawatt laser facilities has reached 8 GeV [5]. Such electron accelerators have wide applications and hold great potential for driving novel radiation sources with ultrahigh time resolution and brilliance, such as betatron radiation [6–9], Thomson scattering photon sources [10], and Compton scattering gamma rays [11–14].

A supersonic gas-jet target has unique significance in producing high-quality electron beams through a laser wakefield. This type of target has a flat top area and sharp boundary, effectively improving the stability of electron beams and reducing the energy spread [15–17]. By adjusting the density profile of the gas jet, the plasma profile can be controlled, electrons injected into the wake field can be restricted in the accelerating phase, and higher energy can be obtained [18, 19]. Furthermore, this target can also be used in laser wakefield acceleration (LWFA) experiments with a high repetition rate [20, 21]. Based on its practicability, multiple simulations [22], designs, and measurements have been conducted [23–25]. Most of the targets provide a density of  $10^{18}$ – $10^{19}$  cm<sup>-3</sup>, and the peak density has reached approximately  $10^{20}$  cm<sup>-3</sup> [26]. An optical interference system is commonly applied to diagnose the gas jet, which can provide accurate results, such as a Mach–Zehnder interferometer [27–29], Michelson

interferometer [30], and other novel interferometers [31]. In fact, owing to space limitations and the high diagnostic accuracy requirements, a small-scale interference diagnosis system with high stability and real-time acquisition is more desirable for experiments. With such diagnosis systems, interference images containing gas target information can be obtained, and after phase extraction and relevant calculations, the required density profile can be obtained as well. Gas jets with various density profiles are required in LWFA, owing to the different mechanisms of electron injection and acceleration. The key parameters affecting the target density profile include the back pressure, nozzle structure, and gas type. These parameters directly affect the length and intensity of the generated laser wakefield, thus changing the energy, charge, energy spread, and other characteristics of the obtained electron beam. Therefore, to acquire high-quality electron beams, it is essential to systematically study the influence of different parameters on the properties of gas targets.

In this study, several supersonic gas jet targets with different structures were proposed. The effects of key parameters on the characteristics of the targets were investigated, such as nozzle throat size, outlet size, gas back pressure, and gas type. Moreover, the relationship between the gas density profile and related parameters was analyzed. We chose a modified Nomarski interference system with high resolution and stability for optical diagnosis to provide accurate results. By adjusting the key parameters, a gas jet with a controllable density profile can be obtained. These targets are expected to be used in LWFA experiments on TW–PW laser facilities in scientific institutions, such as the Shanghai Institute of Optics and Mechanics, Shanghai Jiaotong University, and Peking University, to provide suitable experimental targets. At the China Institute of Atomic Energy, a 100 TW ultrashort-pulse laser facility is nearing completion. The generation of betatron radiation and Compton scattering source will be studied based on high-quality electrons produced by the developed supersonic gas-jet targets.

## 2 Experiment setup

To obtain a quasi-monoenergetic electron beam with higher energy and lower energy spread in the LWFA experiment, the density profile of the gas jet requires a sharp boundary and a nearly flat-top area. We have developed gas nozzles with a de Laval structure to produce this type of gas jet, as shown in Fig. 1. Such nozzles are comprised of convergent sections, divergent sections, and throats. The gas flow is accelerated from the convergent section, reaches the speed of sound at the throat, enters the divergent section, and continues to accelerate to reach

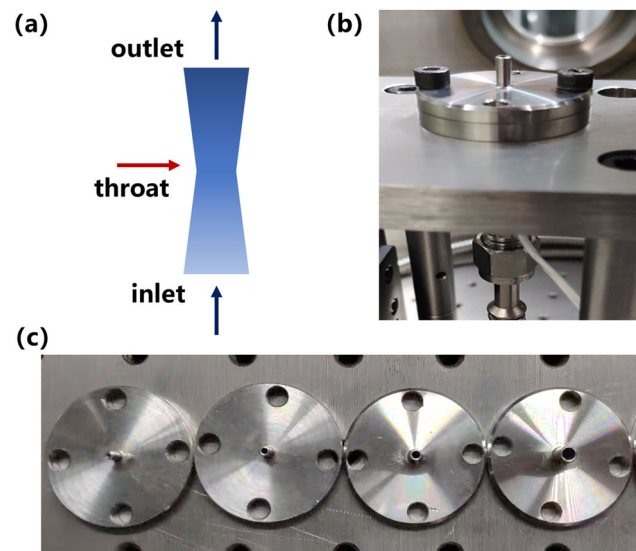
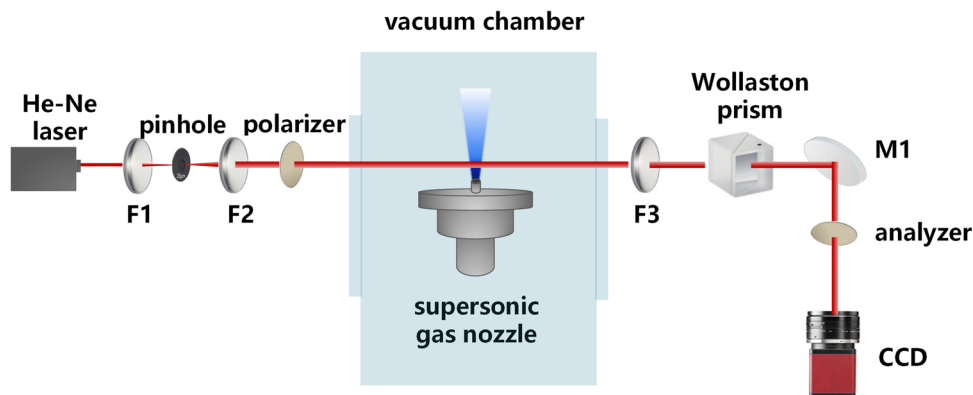


**Fig. 1** (Color online) Supersonic gas-jet targets with different structures proposed: **a** schematic layout of de Laval structure, **b** gas target located in cylindrical vacuum chamber, and **c** targets developed with different outlet sizes for LWFA experiments (0.75 mm/1 mm/1.5 mm/2 mm)

supersonic speed. Conical nozzles with various throat sizes and outlet sizes were developed to investigate the effect of different parameters on the target characteristics. The convergent and divergent sections of the nozzles are conical, which is convenient for obtaining supersonic uniform gas jets. The minimum throat diameters are 0.5 mm and 1 mm, respectively, and the nozzles have a variety of outlet sizes from submillimeter to millimeter (0.75 mm/1 mm/1.5 mm/2 mm). The target was located in a cylindrical vacuum chamber, and the position was adjusted using a three-axis stage. The gases used in the experiment include high-purity helium, nitrogen, and argon supplied to the nozzle from a high-pressure pipeline. The gas jet is precisely controlled by a pulse valve with a high-speed response time of hundreds of microseconds. The valve has high repeatability and is suitable for providing supersonic gas jets for LWFA with high repetition rates.

By setting up a modified Nomarski interference system with vertical fringes, the density profile of the gas target can be determined. The system has a strictly equal optical path, high stability, and real-time acquisition, guaranteeing the integrity and accuracy of the gas jet imaged on the interference area. The performance of this system was studied in our previous work [32]. The system is illustrated in Fig. 2. A He-Ne laser with a wavelength of 632.8 nm was chosen as the probe laser, and a pinhole was set as a spatial filter to improve the beam quality. The beam was linearly polarized by a polarizer and passed through the gas region in the vacuum chamber. The laser beam was divided into ordinary light (o-light) and extraordinary light (e-light)

**Fig. 2** (Color online) Schematic layout of the modified Nomarski interference system for gas-jet diagnosis. The probe laser passes through the gas jet region above the nozzle and is divided into two beams by the Wollaston prism. The interferogram is finally imaged on the CCD, and phase-shift images can be extracted



by a Wollaston prism with a small separation angle. We chose a Wollaston prism with a clear aperture of  $\phi 10$  mm and a separation angle of  $1^{\circ}20'$ . Such conditions ensure that the entire laser beam passes through the prism completely and acquires a sufficient interference fringe area to diagnose the gas target. The polarization was adjusted to be consistent using an analyzer. The interference fringes appeared at the overlapping region of o-light and e-light and were finally imaged on a CCD. The fringe spacing and direction could be controlled by adjusting the positions and angles of the Wollaston prism and analyzer. In the experiments, we adjusted the interference fringes in the vertical direction to obtain accurate gas jet information. To obtain higher-contrast interferograms, we set the angle of the polarizer to  $140^{\circ}$ , the angle of the Wollaston prism to  $95^{\circ}$ , and the angle of the analyzer to  $50^{\circ}$ . The pixel size of the imaging CCD was  $3.69 \mu\text{m} \times 3.69 \mu\text{m}$ , with a resolution of  $3384 \times 2710$ . Accurate time synchronization between the CCD shutter and gas jet was realized using a digital delay and pulse generator DG535. Using the established Nomarski interference system, interference images of the supersonic gas-jet target can be obtained. After phase extraction and calculation, the density profiles of the gas jets under different parameters were obtained.

### 3 Analysis

The supersonic gas jet was ejected from the nozzle outlet when the pulse valve was opened. The presence of gas causes a density change above the nozzle, thus affecting the refractive index. For the Nomarski interference system with vertical fringes, the width of the fringes changes accordingly, which indicates the variation of the phase shift. This is the main principle of optical diagnosis systems. In this section, we describe the data analysis method and the diagnostic ability of the system.

The established coordinate system is illustrated in Fig. 3. The  $x$ -axis is defined as perpendicular to the fringe

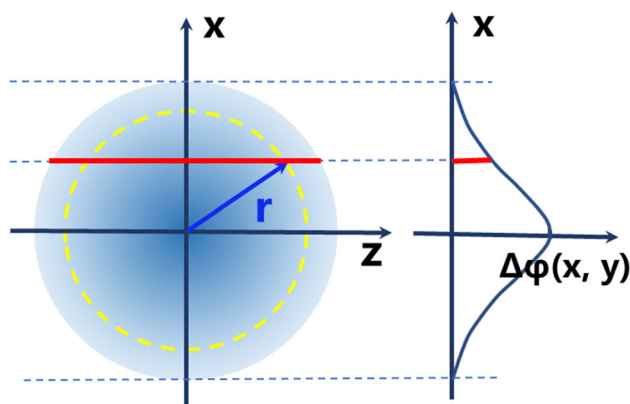


**Fig. 3** (Color online) Schematic of the relationship between the refractive index and phase shift of the axisymmetric gas-jet section. The phase shift  $\Delta\phi(x, y)$  is calculated by integrating the refractive index along different paths

direction, the  $y$ -axis is defined along the fringe direction, and the  $z$ -axis is the laser transmission direction. In our Nomarski system, the interferogram is produced by the overlapping of o-light and e-light separated by the Wollaston prism. The two beams can be seen as the probe laser coming from two virtual foci and having exactly the same optical path. We collected interferograms with and without gas jets, and the phase shift can be extracted by processing these images, as shown in Fig. 4. The change in the refractive index causes a change in the optical path length, which can be expressed by a phase shift. The optical path shift can be described by:

$$\delta = (\eta_2 - \eta_1)l, \tag{1}$$

where  $l$  is the optical path length, and  $\eta_1$  and  $\eta_2$  are the refractive indices of the vacuum and gas jets, respectively. Because the density of the gas jet is not uniform, the optical path shift  $\delta$  can be calculated by integrating through the gas region:

$$\delta(x, y) = \int [\eta_2(x, y, z) - \eta_1(x, y, z)]dz. \tag{2}$$

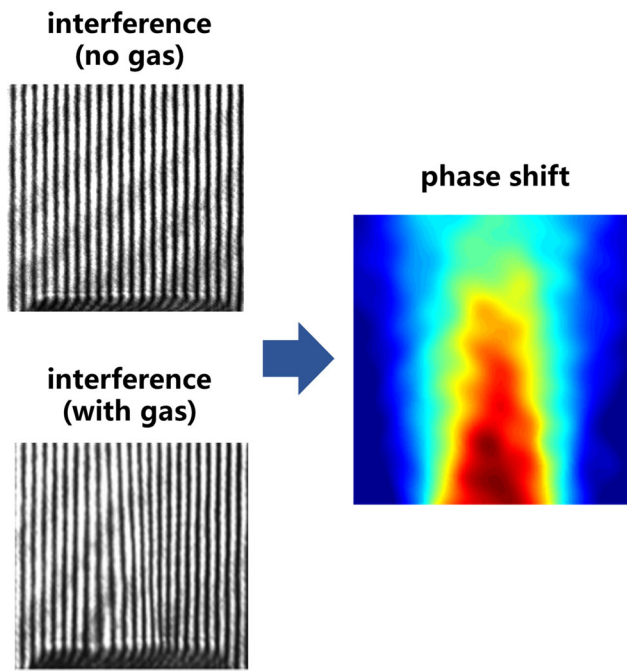


**Fig. 4** (Color online) The presence of gas will change the width of interference fringes, and the phase shift can be extracted by processing the interferograms with and without gas jets

Therefore, the relationship between the phase shift  $\Delta\varphi$  and the refractive index can be expressed as

$$\begin{aligned} \Delta\varphi(x, y) &= \frac{2\pi}{\lambda} \delta(x, y) \\ &= \frac{2\pi}{\lambda} \int_{-\infty}^{\infty} [\eta_2(x, y, z) - \eta_1(x, y, z)] dz, \end{aligned} \tag{3}$$

where  $\lambda$  denotes the wavelength of the laser. For the proposed conical nozzles with a centrosymmetric structure, as shown in Fig. 1, Eq. (3) can be transformed into the following expression:

$$\Delta\varphi(x, y) = \frac{4\pi}{\lambda} \int_x^{\infty} \frac{[\eta_2(y, r) - \eta_1(y, r)]}{\sqrt{r^2 - x^2}} dr. \tag{4}$$

This process is called the Abel transition. From Fig. 3, it is obvious that  $r = \sqrt{(x^2 + z^2)}$ . By inverting the Abel transition, the refractive index can be expressed as [33, 34]

$$\eta_2(y, r) - \eta_1(y, r) = -\frac{\lambda}{2\pi^2} \int_r^{\infty} \frac{\partial\Delta\varphi(x, y)}{\partial x} \frac{1}{\sqrt{x^2 - r^2}} dx. \tag{5}$$

By processing the intensity information of the interferograms with and without a gas jet, the phase shift can be obtained by using the inverse Fourier transform and arctangent function:

$$\begin{aligned} \Delta\varphi(x, y) &= \tan^{-1} \left( \frac{\sin(\Delta\varphi(x, y))}{\cos(\Delta\varphi(x, y))} \right) \\ &= \tan^{-1} \left( \frac{\Im c(x, y)}{\Re c(x, y)} \right), \end{aligned} \tag{6}$$

$c(x, y)$  is directly extracted from the expression of the interference pattern. A detailed analysis can be found in our previous work [32]. The relationship between the refractive index and phase shift can be calculated by substituting Eq. (6) into Eq. (5).

The dependence between the particle density  $n$  and refractive index  $\eta$  is given by the Lorentz–Lorenz equation [35, 36]:

$$\frac{\eta^2 - 1}{\eta^2 + 2} = \frac{n\alpha}{3\epsilon_0}, \tag{7}$$

where  $\alpha$  is the polarizability of the gas atoms and  $\epsilon_0$  is the permittivity of vacuum. The polarizabilities and refractive indices of the different gases are listed in Table 1. In a vacuum environment, the refractive index can be approximated as 1, and Eq. (7) can be simplified as

$$n = \frac{2\epsilon_0}{\alpha} (\eta - 1). \tag{8}$$

Finally, by substituting in Eq. (8), the particle density of the gas jet can be calculated as

$$n(y, r) = -\frac{\epsilon_0\lambda}{2\pi^2\alpha} \int_r^{\infty} \frac{\partial\Delta\varphi(x, y)}{\partial x} \frac{1}{\sqrt{x^2 - r^2}} dx. \tag{9}$$

As shown in Table 1, the refractive indices of the different gases varied over a wide range. Gases with a lower refractive index, such as hydrogen and helium, cannot produce obvious phase shifts under the same conditions. This requires an optical diagnosis system to provide a higher resolution to identify minute changes in interference fringes. To ensure the accuracy of the experimental results, we verified the performance of the established Nomarski interference diagnosis system.

In the experiment, we selected helium, nitrogen, and argon, which have different refractive indices and are often

**Table 1** Reference values of refractive index and polarizability

Gas type	Refractive index	Polarizability (F m <sup>2</sup> )
He	$3.492 \times 10^{-5}$	$2.300 \times 10^{-41}$
Ne	$6.712 \times 10^{-5}$	$4.421 \times 10^{-41}$
H <sub>2</sub>	$13.88 \times 10^{-5}$	$9.143 \times 10^{-41}$
Ar	$28.12 \times 10^{-5}$	$18.52 \times 10^{-41}$
N <sub>2</sub>	$29.79 \times 10^{-5}$	$19.62 \times 10^{-41}$

used in LWFA experiments. The nozzle was located at the bottom center of the interferograms, and the gas jet was ejected from the bottom to the top. The back pressure was maintained at 25 bar. By extracting the phase shifts from

multiple sets of interferograms and analyzing them by Abel inversion, we can calculate the density profile of the gas jet. As shown in Fig. 5, the phase-shift images and density profiles of three different supersonic gas jets were

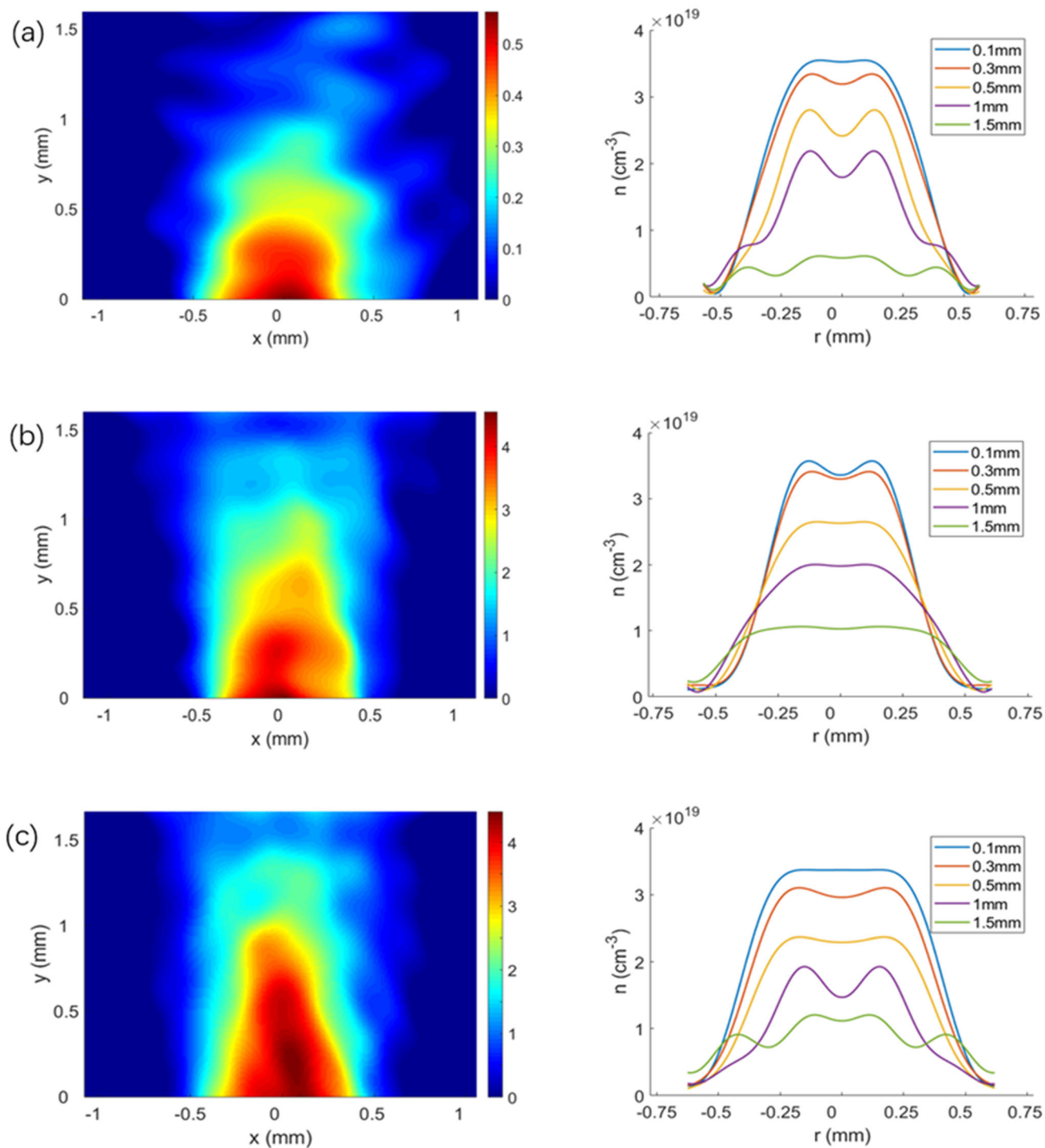


**Fig. 5** (Color online) The phase shift and density profile images of gases with different refractive indices through the Nomarski interference diagnosis system: **a** images of helium (He), **b** images of nitrogen (N<sub>2</sub>), and **c** images of argon (Ar). Helium has the lowest

phase shift, whereas nitrogen and argon have approximately equal phase shifts. The color bars in the right column represent the distance from the nozzle outlet

successfully obtained. The basic outline of the gas jet can be observed in the phase-shift image. For supersonic gas jets, the sharp boundary and uniform density profile can be maintained for several millimeters from the nozzle outlet, providing unique advantages for high-quality electron beams. As shown in Table 1, helium has the lowest refractive index, and thus, the phase shift of its gas jet is also the lowest among the three. Because of the similar refractive indices of nitrogen and argon, their phase shifts are also very similar. According to the Lorentz–Lorenz equation, the gas density is related to the refractive index and polarizability, and the gas type does not affect the density under the same external conditions. Our experimental results are consistent with this principle. The three density profiles obtained by the Abel inversion are identical. This demonstrates the diagnostic ability of the Nomarski interference system on various supersonic gas-jet targets commonly used in LWFA.

#### 4 Results and discussion

To investigate the influence of nozzle structure on gas jet density, nozzles with a throat size of 0.5 mm and different outlet diameters of 0.75, 1.0, and 1.5 mm were developed. As shown in Fig. 6, the nozzles produce gas jets with flat-top density profiles and a sharp gradient according to the characteristics of the supersonic gas jet. In comparison, the size of the outlet clearly affects the density profile. With argon under a back pressure of 25 bar, the maximum densities of the three gas jets directly above the nozzle outlet were  $5.1 \times 10^{19}$ ,  $3.5 \times 10^{19}$ , and  $1.3 \times 10^{19}$   $\text{cm}^{-3}$ . These results are consistent with the quasi-one-dimensional analysis of fluid dynamics:

$$\frac{A^*}{A} = Ma \left[ 1 + \frac{\gamma - 1}{\gamma + 1} (Ma^2 - 1) \right]^{-\frac{\gamma + 1}{2(\gamma - 1)}}, \quad (10)$$

$$\frac{T_0}{T} = 1 + \frac{\gamma - 1}{2} (Ma^2), \quad (11)$$

$$\frac{n_0}{n} = \left[ 1 + \frac{\gamma - 1}{2} (Ma^2) \right]^{\frac{1}{\gamma - 1}}, \quad (12)$$

$$\frac{p_0}{p} = \left[ 1 + \frac{\gamma - 1}{2} (Ma^2) \right]^{\frac{\gamma}{\gamma - 1}}, \quad (13)$$

$A^*$  and  $A$  represent the area of the nozzle cross-section at the throat and any other position,  $Ma$  is the Mach number, and  $\gamma$  is the adiabatic index of the gas. The value of  $\gamma$  is  $5/3$  for monatomic gases and  $7/5$  for diatomic gases. Equation (10) gives the decisive factor for the Mach number. Accordingly, in the de Laval structure, the Mach number is 1 at the throat of the nozzle, and the gas flow velocity

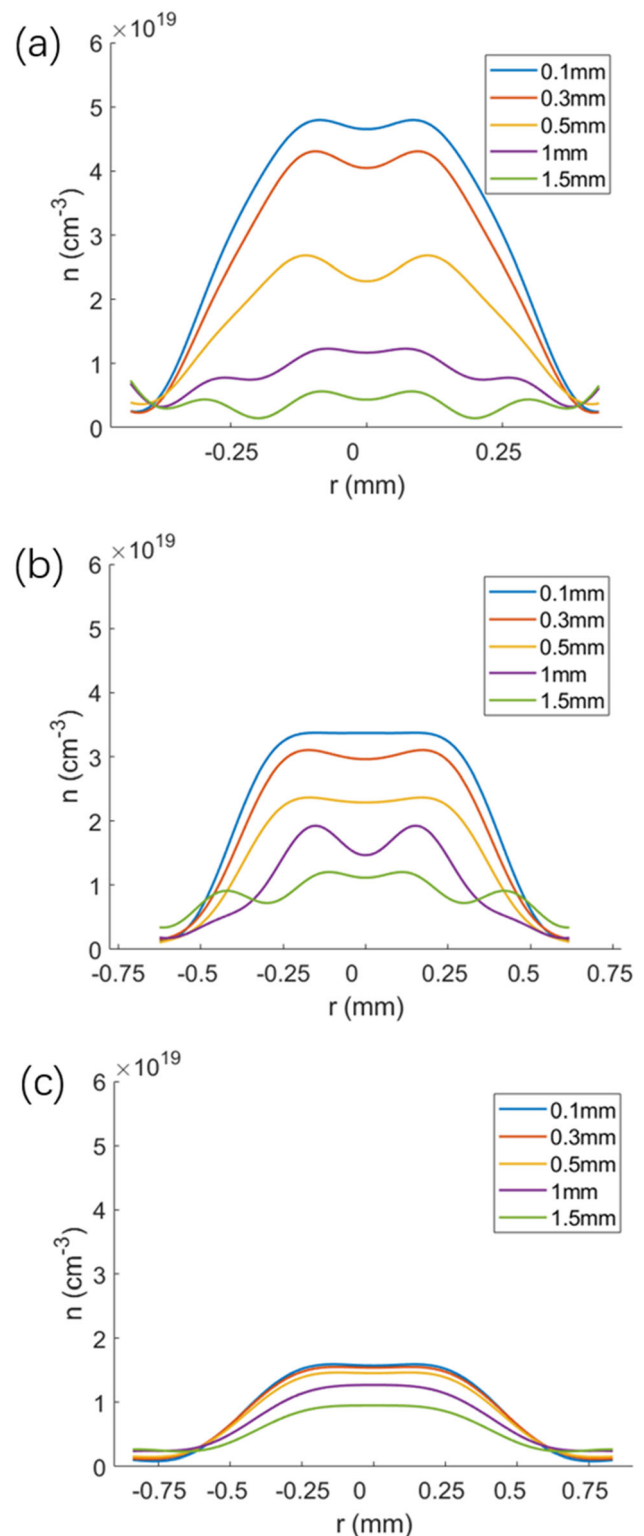


**Fig. 6** (Color online) Density profiles of three nozzles with different outlet sizes: **a** density profiles of the nozzle with outlet diameter of 0.75 mm, **b** density profiles of the nozzle with outlet diameter of 1 mm, and **c** density profiles of the nozzle with outlet diameter of 1.5 mm. The density profiles at different distances from the outlet are also provided

reaches sonic speed. When entering the divergent section, the Mach number exceeds 1, resulting in a supersonic gas jet and continuous acceleration. Equations (11)–(13) describe the influence of the Mach number on the temperature ( $T$ ), density ( $n$ ), and pressure ( $p$ ) of the gas jet under quasi-one-dimensional conditions. When an isentropic expansion occurs in the nozzle, the decisive parameters mentioned above can be expressed by the Mach number. In the equations,  $T_0$ ,  $n_0$ , and  $p_0$  are the initial temperature, density, and pressure at the nozzle inlet, respectively.

Equation (12) indicates the relationship between gas density and Mach number. When the external conditions were consistent, they were inversely proportional. This is consistent with our experimental results. Under the same throat size, the gas nozzle with 0.75 mm outlet diameter has the smallest Mach number, such that it can produce the highest gas density among the three nozzles. The overall density of the gas jet decreases with an increase in outlet size. Meanwhile, owing to the diffusion of the gas jet, the density profile gradually decreases with increasing distance from the nozzle outlet. The density profile at the distances of 0.1, 0.3, 0.5, 1, and 1.5 mm from the outlet were obtained. At a distance of 0.5 mm from the outlet, the maximum densities of the three nozzles decrease to  $3.2 \times 10^{19}$ ,  $2.7 \times 10^{19}$ , and  $0.9 \times 10^{19} \text{ cm}^{-3}$ , respectively. Furthermore, nozzles with different outlet diameters can provide different flat-top widths, and the widths of the three nozzles at the outlet are 0.35, 0.54, and 0.76 mm, respectively. Some small-scale floating in the flat-top area is mainly caused by the secondary interference introduced by the optical lens and the calculation singularity of the Abel inversion.

We also compared the effects of different throat sizes on the characteristics of the gas jet. Gas nozzles with 0.5 and 1 mm throats were tested. For variable control, both nozzles had an outlet diameter of 2 mm, and the back pressure was controlled at 25 bar. The density profiles of two gas jets at different distances from the nozzle outlet were obtained (0.1, 0.3, 0.5, 1, 1.5, and 3 mm) at different distances from the nozzle outlet. According to Eq. (12), the gas nozzle with a narrower throat diameter has a larger Mach number and lower gas density, which was verified in our experiments. As shown in Fig. 7, the maximum gas jet densities of the two nozzles were  $5.62 \times 10^{18} \text{ cm}^{-3}$  and  $9.16 \times 10^{18} \text{ cm}^{-3}$ , respectively. Based on the results, the nozzle with a 0.5 mm throat produces a lower density. In terms of the nozzle structure, those with a narrower throat and wider outlet size produce supersonic gas jets with higher velocity and lower density. Therefore, by adjusting the structure of the nozzle outlet and throat, the gas density can be controlled to meet the requirements of the experiment.

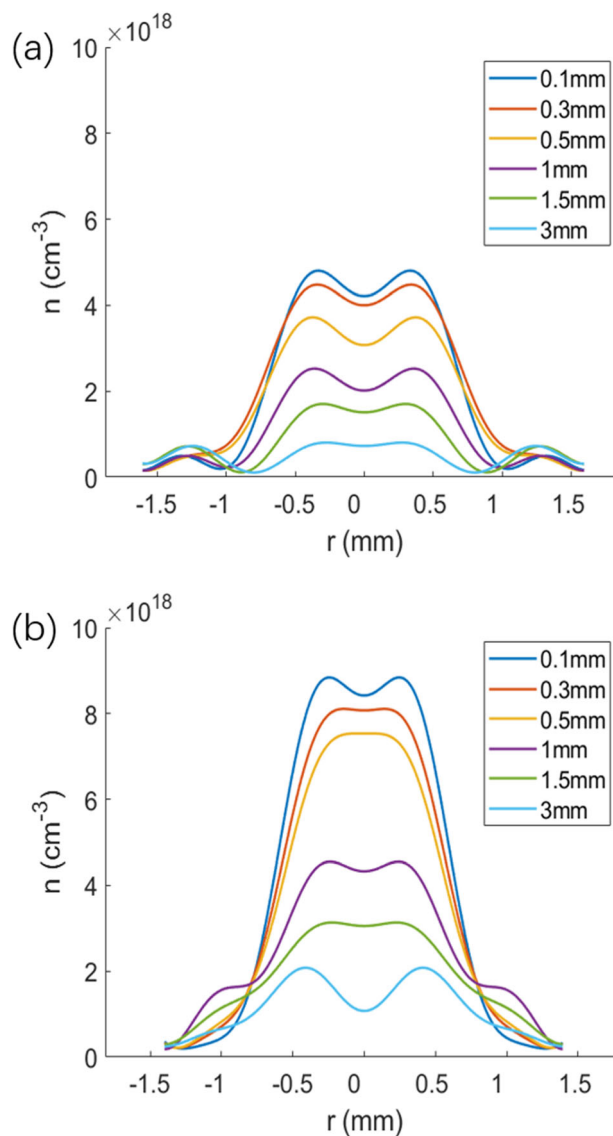


**Fig. 7** (Color online) Density profiles at different distances from the nozzles with different throats: **a** nozzle with throat diameter of 0.5 mm and **b** nozzle with throat diameter of 1 mm

In actual LWFA experiments, because the gas-jet target is commonly placed in a large chamber with a high vacuum degree, it will take a long time to replace the target frequently, which is also not conducive to maintaining the vacuum degree. Therefore, back pressure control is one of the most practical methods for adjusting the gas jet density, which can be directly implemented outside the vacuum chamber. Because back pressure is an important parameter affecting the gas density, to study the relationship between them, we measured the gas density of nozzles with different outlet sizes under a back pressure of 10–40 bar. Figure 8 shows the flat-top density in the same center region of the gas jets at various back pressures. From the experimental results, it can be seen that with the increase in

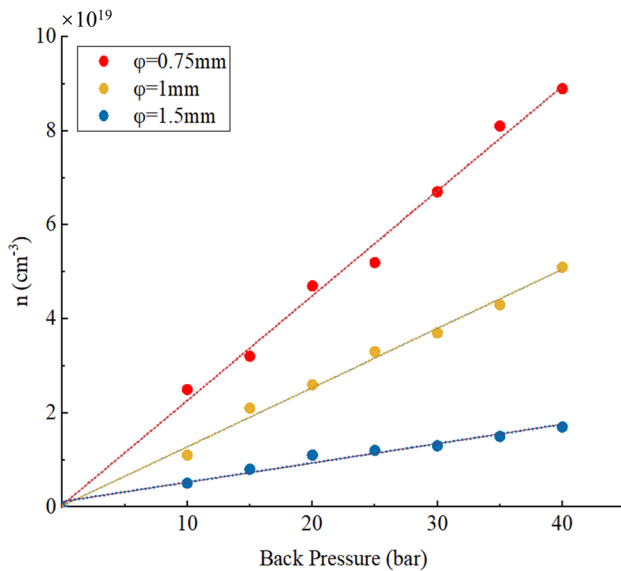


**Fig. 8** (Color online) The relationship between back pressure and gas-jet density. Three nozzles with different outlet sizes were tested, and the back pressure ranged from 10 to 40 bar

back pressure, the gas density increases gradually, and the nozzle with a smaller outlet exhibits greater changes in density. The gas density scale was linearly proportional to the operating back pressure. Theoretically, as derived from Eqs. (12) and (13), the density has a power-law dependence on the back pressure. Nevertheless, within a certain range, we can approximately describe them as being linearly related. This can serve as the basis of back-pressure adjustment for specific gas profile requirements in LWFA.

## 5 Conclusion

In this work, we investigated the effective parameters of supersonic gas-jet targets used in LWFA experiments. Gas density profiles with different throat sizes, outlet sizes, and back pressures were measured. The gas jets show flat-top regions and sharp boundaries with a high gradient, and the density can be adjusted in the range of  $10^{17}$ – $10^{19}$   $\text{cm}^{-3}$ . We have provided the profiles of the gas density at different regions above the nozzle outlet. When the laser interacts with the gas jet, the characteristics of the wakefield can be controlled by regulating the laser incident position above the nozzle. Moreover, the relationship between gas density and back pressure has been presented, which can be used as an important basis for adjusting the gas density in electron acceleration experiments. With the modified Nomarski interference system, high-resolution diagnosis of gases with different refractive indices was realized. Based on the results, supersonic gas-jet targets with an adjustable density profile can be used to generate the required electron beams

in LWFA experiments. Such high-quality electron beams are expected to support further research on new radiation sources driven by ultrashort and ultraintense lasers.

**Author Contributions** All authors contributed to the study conception and design. Experiment was carried out by Qiu-Shi Liu, Ming-Jiang Ma, Bao-Zhen Zhao, Xiao-Hua Zhang, Xiang-Hao Meng, and Xiao-Na Ban. Data analysis was performed by Qiu-Shi Liu, Bing Guo, Chong Lv, Ji Zhang, Bao-Xian Tian, and Chuang-Ye He. Optical diagnosis system was set up by Qiu-Shi Liu, Ming-Jiang Ma, Zhao Wang, and Xiao-Feng Xi. The first draft of the manuscript was written by Qiu-Shi Liu, and all authors commented on previous versions of the manuscript. All authors read and approved the final manuscript.

## References

- G.A. Mourou, T. Tajima, S.V. Bulanov, Optics in the relativistic regime. *Rev. Mod. Phys.* **78**, 309 (2006). <https://doi.org/10.1103/RevModPhys.78.309>
- T. Tajima, J.M. Dawson, Laser electron accelerator. *Phys. Rev. Lett.* **43**, 267 (1979). <https://doi.org/10.1103/PhysRevLett.43.267>
- E. Esarey, C.B. Schroeder, W.P. Leemans, Physics of laser-driven plasma-based electron accelerators. *Rev. Mod. Phys.* **81**, 1229 (2009). <https://doi.org/10.1103/RevModPhys.81.1229>
- X. Wang, R. Zgadzaj, N. Fazel et al., Quasi-monoenergetic laser-plasma acceleration of electrons to 2 GeV. *Nature Commun.* **4**, 1988 (2013). <https://doi.org/10.1038/ncomms2988>
- A.J. Gonsalves, K. Nakamura, J. Daniels et al., Petawatt laser guiding and electron beam acceleration to 8 GeV in a laser-heated capillary discharge waveguide. *Phys. Rev. Lett.* **122**, 084801 (2019). <https://doi.org/10.1103/PhysRevLett.122.084801>
- A. Rousse, K.T. Phuoc, R. Shah et al., Production of a keV X-ray beam from synchrotron radiation in relativistic laser-plasma interaction. *Phys. Rev. Lett.* **93**, 135005 (2004). <https://doi.org/10.1103/PhysRevLett.93.135005>
- S. Corde, K.T. Phuoc, G. Lambert et al., Femtosecond x rays from laser-plasma accelerators. *Rev. Mod. Phys.* **85**, 1–48 (2013). <https://doi.org/10.1103/RevModPhys.85.1>
- K.T. Phuoc, S. Corde, R. Shah et al., Imaging electron trajectories in a laser-wakefield cavity using betatron x-ray radiation. *Phys. Rev. Lett.* **97**, 225002 (2006). <https://doi.org/10.1103/PhysRevLett.97.225002>
- Y. Lu, G. Zhang, J. Zhao et al., Ultra-brilliant GeV betatronlike radiation from energetic electrons oscillating in frequency-downshifted laser pulses. *Opt. Express* **29**, 6 (2021). <https://doi.org/10.1364/OE.419761>
- S.G. Rykovanov, C.G.R. Geddes, J.-L. Vay et al., Quasi-monoenergetic femtosecond photon sources from Thomson Scattering using laser plasma accelerators and plasma channels. *J. Phys. B AT Mol. Opt.* **47**, 23 (2014). <https://doi.org/10.1088/0953-4075/47/23/234013>
- E. Irani, H. Omidvar, R. Sadighi-Bonabi, Gamma rays transmutation of Palladium by bremsstrahlung and laser inverse Compton scattering. *Energ. Convers. Manage.* **77**, 558 (2014). <https://doi.org/10.1103/RevModPhys.78.3091>
- D. Li, K. Imasaki, K. Horikawa et al., Iodine transmutation through laser Compton scattering gamma rays. *J. Nucl. Sci. Technol.* **46**, 8 (2009). <https://doi.org/10.3327/jnst.46.831>
- H. Xu, H. Wu, G. Fan et al., A new consecutive energy calibration method for X/γ detectors based on energy continuously

- tunable laser Compton scattering light source. *Nucl. Sci. Tech.* **28**, 121 (2017). <https://doi.org/10.1007/s41365-017-0272-1>
14. X. Zhu, M. Chen, S. Weng et al., Extremely brilliant GeV  $\gamma$ -rays from a two-stage laser-plasma accelerator. *Sci. Adv.* **6**, 22 (2020). <https://doi.org/10.1126/sciadv.aaz7240>
  15. C.G.R. Geddes, C. Toth, J. Van Tilborg et al., High-quality electron beams from a laser wakefield accelerator using plasma-channel guiding. *Nature* **431**, 538 (2004). <https://doi.org/10.1038/nature02900>
  16. J. Faure, Y. Glinec, A. Pukhov et al., High-charge energetic electron bunch generated by 100 TW laser pulse. *Nature* **431**, 541 (2004). <https://doi.org/10.1038/nature02963>
  17. S.P.D. Mangles, C.D. Murphy, Z. Najmudin et al., Particle acceleration using intense laser produced plasmas. *Nature* **431**, 535 (2004). <https://doi.org/10.1038/nature02939>
  18. F. Sylla, A. Flacco, S. Kahaly et al., Short intense laser pulse collapse in near-critical plasma. *Phys. Rev. Lett.* **110**, 085001 (2013). <https://doi.org/10.1103/PhysRevLett.110.085001>
  19. W. Wang, W. Li, J. Liu et al., High-brightness high-energy electron beams from a laser wakefield accelerator via energy chirp control. *Phys. Rev. Lett.* **117**, 124801 (2016). <https://doi.org/10.1103/PhysRevLett.117.124801>
  20. F. Salehi, A.J. Goers, G.A. Hine et al., MeV electron acceleration at 1 kHz with <10 mJ laser pulses. *Optics Lett.* **42**, 2 (2017). <https://doi.org/10.1364/OL.42.000215>
  21. D. Guenot, D. Gustas, A. Vernier et al., Relativistic electron beams driven by kHz single-cycle light pulses. *Nat. Photonics* **11**, 5 (2017). <https://doi.org/10.1038/nphoton.2017.46>
  22. K. Schmida, L. Veisz, Supersonic gas jets for laser-plasma experiments. *Rev. Sci. Instrum.* **83**, 053304 (2012). <https://doi.org/10.1063/1.4719915>
  23. B. Landgraf, M. Schnell, A. Savert et al., High resolution 3D gas-jet characterization. *Rev. Sci. Instrum.* **82**, 083106 (2011). <https://doi.org/10.1063/1.3624694>
  24. V. Malka, C. Coulaud, J.P. Geindre et al., Characterization of neutral density profile in a wide range of pressure of cylindrical pulsed gas jets. *Rev. Sci. Instrum.* **71**, 2329 (2000). <https://doi.org/10.1063/1.1150619>
  25. S. Lorenz, G. Grittani, E. Chacon-Golcher et al., Characterization of supersonic and subsonic gas targets for laser wakefield electron acceleration experiments. *Matter. Radiat. Extremes* **4**, 015401 (2019). <https://doi.org/10.1063/1.5081509>
  26. F. Sylla, M. Veltcheva, S. Kahaly et al., Development and characterization of very dense submillimetric gas jets for laser-plasma interaction. *Rev. Sci. Instrum.* **83**, 033507 (2012). <https://doi.org/10.1063/1.3697859>
  27. A.M. Hansen, D. Haberberger, J. Katz et al., Supersonic gas-jet characterization with interferometry and Thomson scattering on the OMEGA Laser System. *Rev. Sci. Instrum.* **89**, 10C103 (2018). <https://doi.org/10.1063/1.5036645>
  28. X. Jun, H. Feng, C. Zhong et al., Super-resolution of interference pattern with independent laser beams. *Chin. Phys. Lett.* **22**, 2824 (2005). <https://doi.org/10.1088/0256-307X/22/11/027>
  29. X. Yang, A new Mach-Zehnder interferometer to measure light beam dispersion and phase shift. *Chin. Phys. Lett.* **30**, 040701 (2013). <https://doi.org/10.1088/0256-307X/30/4/040701>
  30. J. Nejdil, J. VanCura, K. Bohacek et al., Imaging Michelson interferometer for a low-density gas jet characterization. *Rev. Sci. Instrum.* **90**, 065107 (2019). <https://doi.org/10.1063/1.5098084>
  31. S. Feister, J.A. Nees, J.T. Morrison et al., A novel femtosecond-gated, high-resolution, frequency-shifted shearing interferometry technique for probing pre-plasma expansion in ultra-intense laser experiments. *Rev. Sci. Instrum.* **85**, 11D602 (2014). <https://doi.org/10.1063/1.4886955>
  32. Q. Liu, M. Ma, X. Zhang et al., Application of Nomarski interference system in supersonic gas-jet target diagnosis. *AIP Adv.* **11**, 015145 (2021). <https://doi.org/10.1063/5.0027317>
  33. G. Pretzier, A new method for numerical Abel-inversion. *Zeitschrift für Naturforschung A* **46**, 639-641 (1991). <https://doi.org/10.1515/zna-1991-0715>
  34. L.M. Smith, D.R. Keefer, S.I. Sudharsanan, Abel inversion using transform techniques. *J. Quant. Spectrosc. Radiat. Transf.* **39**, 367-373 (1988). [https://doi.org/10.1016/0022-4073\(88\)90101-X](https://doi.org/10.1016/0022-4073(88)90101-X)
  35. H.A. Lorentz, Ueber die Beziehung zwischen der Fortpflanzungsgeschwindigkeit des Lichtes und der Körperdichte. *Ann. Phys.* **245**, 641-655 (1880). <https://doi.org/10.1002/andp.18802450406>
  36. L. Lorenz, Ueber die Refraktionsconstante. *Ann. Phys.* **247**, 70-103 (1880). <https://doi.org/10.1002/andp.18802470905>